

# ISOLATED FLUID OXYGEN DROP BEHAVIOR IN FLUID HYDROGEN AT ROCKET CHAMBER PRESSURES

K. Harstad and J. Bellan  
Jet Propulsion Laboratory  
California Institute of Technology  
Pasadena, CA. 91109

## Abstract

A model has been developed for the behavior of an isolated fluid drop of a single compound immersed into another compound in finite, quiescent surroundings at supercritical conditions. The model is based upon fluctuation theory which accounts for both Soret and Dufour effects in the calculation of the transport matrix relating molar and heat fluxes to the transport properties and the thermodynamic variables. The transport properties have been modeled over a wide range of pressure and temperature variation applicable to  $LO_x - H_2$  conditions in rocket motor combustion chambers. The equations of state have been calculated using a previously-derived, computationally-efficient and accurate protocol. Results obtained for the  $LO_x - H_2$  system show that the supercritical behavior is essentially one of diffusion. The temperature profile relaxes fastest followed by the density and lastly by the mass fraction profile. An effective Lewis number calculated using theory derived elsewhere shows that it is larger by approximately a factor of 40 than the traditional Lewis number. The parametric variations show that gradients increasingly persist with increasing fluid drop size or pressure, and with decreasing temperature. The implication of these results upon accurate measurements of fluid drop size under supercritical conditions is discussed.

## 1. Introduction

Liquid rocket engine design is not a mature technology in that the issues of reliability and efficiency are unresolved. Current designs are still based upon empirical knowledge and theory that does not portray the complexities of the physical processes and of the environment in the combustion chambers. The extensive review on liquid propellant, rocket instabilities compiled by Harrje and Reardon [1] more than twenty years ago remains the base of rocket design despite the increased understanding that many of the approximations made in performing the calculations compromise the validity of the results.

One of the foundations of liquid rocket instabilities is the theory of isolated drop evaporation and combustion in an infinite medium [1], [2]. The early version of that theory was based on the assumption of quasi-steady gas behavior with respect to the liquid phase, an assumption strictly

valid only at low pressures where the liquid density is three orders of magnitude larger than that of the gas. Recognizing that at the elevated pressures of liquid rocket chambers the liquid density approaches that of the gas, the quasi-steady assumption was relaxed in other investigations [3], [4], [5], [6], [7]. However, it is only recently that the description of the full complexity of combustion chambers processes was undertaken; this includes not only the complete unsteady treatment of the conservation equations but also appropriate equations of state with consistent mixing rules and transport properties valid over transcritical/supercritical conditions.

The discussion below emphasizes the  $LO_x$  system because its behavior sometimes contrasts with that observed for hydrocarbons as noted by Chesneau et al. [8]. Therefore, the results of many interesting studies in the context of Diesel engines or high-pressure gas turbine engines will not be discussed. Such a discussion appears in the review of Givler and Abraham [9].

Yang et al. [10] described the vaporization of a liquid oxygen drop ( $LO_x$ ) in hydrogen over a wide range of pressures. The model includes thermodynamic non-idealities, variable properties and the assumption of liquid-vapor phase equilibria. The Soret term accounting for species transport due to thermal gradients and the Dufour term accounting for heat transfer resulting from concentration gradients are neglected. In the side of the drop boundary containing hydrogen, the Soave-Redlich-Kwong (SRK) equation of state (EOS) is used to calculate the compressibility factor while the density of in the  $LO_x$  side of the boundary is given by curve-fitted experimental data. The thermal conductivities and heat capacities are correlated as functions of density and temperature, the liquid diffusivity is estimated following Scheibel's [11] procedure, and the binary diffusion coefficients are calculated following the corresponding states method of Takahashi [12]. Calculations are initiated with a drop at subcritical temperature in surroundings where the pressure and temperature are both above the critical point; once the drop surface temperature reaches the critical point, the assumption is made that it is this surface that continues to define a gas/liquid interracial boundary and thus it is its motion that defines the drop regression rate. This surface tracks thus the progression of a liquid entity composed of both  $LO_x$  and hydrogen in contrast, to the pure  $LO_x$  drop. Plots of the temperature, mole fraction and density all show steep gradients around what is presumably the interface (the interfacial boundary is not indicated on the curves). Because the radial coordinate is logarithmic, it is impossible to compare the detailed evolution of the heat versus the mass transfer; however, plots of the Lewis number show that it reaches values as large as 1.9 on the hydrogen side and 1.3 in the  $LO_x$  side. The results show the increasing importance of hydrogen diffusion into  $LO_x$  and the increase in vaporization rate with increasing pressure. Surprisingly, the results show that the classical, quasi-steady-derived  $D^2$ -law [2] remains valid for all pressures (5-250 atm) and drop diameters ( $5 \times 10^{-6}$ – $300 \times 10^{-6}$  m). Hsiao et al. [13] extended the study of [10] to include convective effects. In this new version, the Benedict-Webb-Rubin (BWR) EOS in conjunction with an extended corresponding states principle, replaces the SRK EOS for the purpose of achieving higher-accuracy density predictions and the corresponding states principle is applied to calculate transport properties. Results from the calculation show that the interface defined by the critical temperature deforms and stretches throughout the drop lifetime presenting a convex surface to the incoming flow. The motion of the drop is defined by the motion of its center of gravity and a drag coefficient is calculated.

The model of Delplanque and Sirignano [14] is similar to that of [10] in that Soret and Dufour effects are neglected and phase equilibrium is assumed; additionally, since the calculations are not pursued beyond the drop surface reaching the critical point, the mixture is approximated by a gas with mixture-averaged properties. The Chueh and Prausnitz [15] version of the Redlich-Kwong

(RK) EOS is used and the thermophysical and transport properties are correlated from data with no correction for real gas behavior. The diffusion coefficients are calculated using dilute gas theory and it is uncertain whether the discussed high-pressure effects [16] are included. The liquid density is evaluated using the Hankinson-Brobst-Thomson method [16] and the isobaric heat capacity is obtained through an ideal gas correlation [16]. Since there is a unique relationship between heat capacities and the enthalpy as expressed by the EOS, it is not clear that this thermodynamic relationship is satisfied by this procedure. Results from the calculations show that the  $LO_x$  drop surface reaches the critical temperature in a time much smaller than the characteristic thermal diffusion time.

More recently, Haldenwang et al. [17] constructed a model similar to those in [10] and [14], but identified the drop surface with the location where thermodynamic equilibrium occurs. The RKSEOS is used in the model and  $C_p$  is estimated independently of the EOS, possibly introducing inconsistencies in the thermodynamics. The binary diffusion coefficients were calculated through empirical correlations [16] in liquids and dense gas, and the thermal conductivity was calculated using standard mixing rules and experimental data for pure substances. In this study, the subcritical regime is defined as that for which the mass fraction at the surface remains higher than that corresponding to the value for which the surface temperature is the critical temperature during the entire drop lifetime. With this definition, the evolution of a  $LO_x$  drop initially at 100 K in surroundings at 1000 K and 8 MPa is classified as subcritical behavior although obviously there is no material drop surface at those conditions. Calculations performed with different thermodynamic properties yield results qualitatively similar but quantitatively different. Just as in [10], the  $D^2$ -law remains valid both in the subcritical and supercritical regimes. Comparisons with the microgravity observations of Sato [18] for n-octane show similar trends: the drop lifetime decreases with increasing pressure in the subcritical regime and increases with increasing pressure in the supercritical regime. To evaluate the impact of the assumed interface location (at the critical temperature [10] versus the saturation temperature [17]), results are presented with the model of [17] using each assumption, and they are further compared with those of [10]; although there is qualitative agreement between the drop lifetime versus the reduced pressure curves found by the authors using each assumption, their variation is not similar to that of [10]. A further detailed evaluation of the influence of the interface definition reveals that, in contrast to the situation when the interface is located at the critical point, an increase in radius is obtained in the transcritical regime when the surface is assumed to be at thermodynamic equilibrium. This effect is attributed to the increase in the difference between equilibrium rim mass fraction and critical mass fraction with increasing pressure. The obvious conclusion from this study is that it is not only the conservation equations, EOS, and transport properties that must be accurately modeled, but also the interface processes.

Haldenwang et al. [17] also note that the results of [10] and [14] for identical conditions have more than one order of magnitude discrepancy, and that their own results do not agree with those of either one of these studies; this indicates that it is only through comparisons with experiments that the cause of the difference could be resolved. However, experiments with  $LO_2$  -- hydrogen combinations are prohibitive and expensive because of the associated safety aspect. Additionally, the interpretation of the results is not straightforward as will be discussed below.

Circumventing the difficulty of  $LO_2$  in hydrogen and that of very high pressures, Chesneau et al. [8] present a set of experiments for  $LO_x$  evaporation in air, nitrogen and helium at 0.1 MPa and 3 MPa. Since the data was acquired through imaging, the drop surface is a measure of steep density gradients. The data shows that at 0.1 MPa, the  $D^2$ -law is validated within the range of

experimental error. In contrast, at 2 MPa the slope of  $D^2$  changes with time, which is documented as an unsteadiness in the evaporation constant; this unsteadiness increases with increasing pressure. These observations seem to disprove the previous theoretical predictions of the  $D^2$ -law holding over the entire subcritical range. More recently, Chauveau and Gökalp [19] acquired data for  $LO_x$  in helium at up to 65 bars under gravity conditions. The drop was suspended from a fiber, indicating that it was not pure  $LO_x$  which becomes super critical (and thus has zero surface tension) at 5.043 MPa. Both sets of data show that the evaporation rate increases with increasing pressure, unlike the data of Sato et al. [18] for n-octane and that of Chauveau et al. [20], [21] for n-heptane and methanol showing a minimum in the evaporation rate at the critical point. Chesneau et al. [8] attempt, to explain the difference between the variation of the evaporation rate of  $LO_x$  and hydrocarbons with pressure on the basis of the reduced temperature in the drops surroundings which in their experiments was supercritical for  $LO_x$  but subcritical for the hydrocarbons. This explanation is not convincing since the data of Sato et al. [18] was acquired for burning n-octane drops and therefore at supercritical surrounding temperature since the critical temperature of n-octane is 570 K. Therefore, the qualitative agreement between Haldenwang et al.'s drop lifetime variation with pressure for  $LO_x$  [17] and the observations of Sato et al. [18] is suspicious and may indicate a flaw in the model rather than a validation of the model.

The above discussion shows that there is still a wide gap between the current modeling capability of  $LO_x$  drops in hydrogen and that necessary for advancing the state of the art in liquid rocket motor design. The model presented below constitutes an improvement over the existing models in that it includes Soret and Dufour effects, and thermodynamic nonequilibrium between phases, none of which were included in [17], [10] and [14]. This set of conservation equations and a kinetic law (equivalent to the Langmuir-Knudsen law that is valid for liquid evaporation) derived here for dense gas are coupled with accurate EOS's and transport coefficients over the subcritical/supercritical range for both  $LO_x$  and hydrogen. The model used for the EOS's has been described in detail elsewhere [22]; these EOS's are obtained by curve fitting data and further extrapolation using the concept of departure function [16]. The importance of Soret and Dufour effects is the subject of discussions in Harstad and Bellan [23] while the thermodynamic equilibrium assumption is shown by Bellan and Summerfield [24] to be unrealistic in certain situations even under subcritical conditions.

## 2. Model

The model of the conservation equations is based on the fluctuation theory of Keizer [25], also described by Peacock-Lopez and Woodhouse [26]. The advantage of this theory is that it inherently accounts for nonequilibrium processes and naturally leads to the most general fluid equations by relating the partial molar fluxes,  $\vec{J}_i$ , and the heat flux,  $\vec{q}$ , to thermodynamic quantities.

### 2.1. Conservation equations

In general form, the conservation equations are:

-continuity

$$\frac{\partial \rho}{\partial t} + \frac{\partial(\rho u_\beta)}{\partial x_\beta} = 0 \quad (2.1)$$

where the conventional index notation for expressing derivatives and sums apply.

-momentum conservation on the  $\alpha$  direction

$$\frac{\partial(\rho u_\alpha)}{\partial t} + \frac{\partial(\rho u_\alpha u_\beta)}{\partial x_\beta} + \frac{\partial p}{\partial x_\alpha} = \frac{\partial \tau_{\alpha\beta}}{\partial x_\beta} \quad (2.2)$$

where  $\tau_{\alpha\beta} = \eta_{mix}[(\partial u_\alpha/\partial x_\beta + \partial u_\beta/\partial x_\alpha) - (2/3)\delta_{\alpha\beta}\partial u_\gamma/\partial x_\gamma]$  is the stress tensor in which  $\delta_{\alpha\beta}$  is a tensor having unit diagonal, its other components being null.

-species conservation

$$\frac{\partial \rho_i}{\partial t} + \frac{\partial(\rho_i u_\beta + m_i J_{i\beta})}{\partial x_\beta} = 0 \quad (2.3)$$

-enthalpy equation

$$\frac{\partial(nh)}{\partial t} + \frac{\partial(nh u_\beta)}{\partial x_\beta} = \frac{\partial p}{\partial t} + u_\beta \frac{\partial p}{\partial x_\beta} - \frac{\partial q_\beta}{\partial x_\beta} + \Phi_v \quad (2.4)$$

where  $\Phi_v = \tau_{\alpha\beta}\partial u_\alpha/\partial x_\beta$  is the viscous dissipation and  $n = p/m$ .

Fluctuation theory relates  $\vec{J}_i$  and  $\vec{q}$  to the transport matrix  $\mathbf{L}$  through

$$\vec{J}_i = L_{iq}\nabla\beta - \sum_j^N L_{ij}\nabla(\beta\mu_j), \quad \vec{q} = L_{qq}\nabla\beta - \sum_j^N L_{qj}\nabla(\beta\mu_j) \quad (2.5)$$

Here  $L_{ij}$  are the Fick's diffusion elements,  $L_{qq}$  is the Fourier thermal diffusion element,  $L_{jq}$  are the Soret diffusion and  $L_{qj}$  are the Dufour diffusion elements and  $\beta \equiv 1/(R_u T)$ . The Onsager relations state that  $L_{ij} = L_{ji}$  and  $L_{iq} = L_{qi}$ . Additionally, conservation of fluxes and mass in the system imply that  $\sum_i^N m_i \vec{J}_i = \vec{0}$  and  $\sum_i^N L_{ij} m_i = 0$  for  $j \in [1, N]$  and  $j = q$ .

Using the thermodynamic relationship

$$d(\beta\mu_j) = \beta(v_j dp - h_j d\ln T) + \left(\sum_1^{N-1} \alpha_{Dji} dX_i\right)/X_j \quad (2.6)$$

where

$$\alpha_{Dij} \equiv \beta X_i \partial \mu_i / \partial X_j = \partial X_i / \partial X_j + X_i \partial \ln \gamma_i / \partial X_j \quad (2.7)$$

one can calculate  $\vec{J}$ , from 2.5 and 2.6.

In general, this formalism proceeds with the definition of a symmetric matrix whose elements are the pair-wise mass diffusion coefficients for the mixture  $D_{mix}^{(ij)}$ , and an antisymmetric matrix whose elements are the thermal diffusion factors  $\alpha_T^{(ij)}$ . For a binary mixture, this formalism simplifies considerably to yield

$$\vec{J}_1 = -(m_2/m)(\vec{J}_a - \mathbf{t} X_1 X_2 \alpha_T n D_m \nabla \ln T) \quad (2.8)$$

$D_m = L_{11} (m/m_2)^2 v / (X_1 X_2)$  is a mass diffusion coefficient,  $\alpha_T = (L_{1q}/L_{11})\beta m_2/m$  is the ratio between the thermal and mass diffusivities, and

$$\vec{J}_a = n D_m \{ \alpha_D \nabla X_1 + \beta [m_1 m_2 X_1 X_2 / m] [(v_1/m_1 - v_2/m_2) \nabla p + (h_2/m_2 - h_1/m_1) \nabla \ln T] \} \quad (2.9)$$

According to Eq. 2.7  $\alpha_D = 1 + X_1(\partial \ln \gamma_1 / \partial X_1)_{T,p}$ , where from the Gibbs-Duhem relationship  $\alpha_{D11} = \alpha_{D22} = -\alpha_{D12} = -\alpha_{D21} = \alpha_D$ . Further, Eq. 2.3 can be simplified to yield

$$\frac{DX_1}{Dt} = -\frac{m}{m_2 n} \nabla \cdot \vec{J}_1 = -\frac{DX_2}{Dt} \quad (2.10)$$

where  $DX_1/Dt \equiv \partial X_1 / \partial t + u_\beta \partial X_1 / \partial x_\beta$ , and  $X_1 = m_2 Y_1 / [m_1 + (m_2 - m_1) Y_1]$ . Combining Eqs. 2.4, 2.8 and 2.9 one obtains

$$nC_p \frac{DT}{Dt} = \alpha_v T \frac{Dp}{Dt} - \nabla \cdot \vec{q} + \Phi_v + m_1 (h_1/m_1 - h_2/m_2) \nabla \cdot \vec{J}_1 \quad (2.11)$$

where  $\alpha_v = [(\partial v / \partial T)_{p,X_1}] / v$  and

$$\vec{q} = -(\alpha_T R_u T) \vec{J}_a - \lambda \nabla T \quad (2.12)$$

Consistent with the previous definitions,  $\lambda = \beta L_{qq} / T$ .

## 2.2. Boundary conditions

Boundary conditions must be applied at three different locations: the fluid drop center, the interface which is initially between the pure  $LO_x$  drop and the fluid, and the far field. In this model, the far field is set at a finite location, which is a multiple of the initial fluid drop radius, from the initial interface. Consistent with previous terminology from subcritical theory [27], this far field location is called the edge of the ‘sphere of influence’ and is located at  $R_{si}$ .

At the center of each entity, spherical symmetry conditions prevail, whereas at the edge of the sphere of influence known conditions apply.

The conditions at the interface express not only conservation of mass, species, momentum and energy, but also nonequilibrium evaporation and solvation. Initially,  $LO_x$  exists for  $r < R_d$  and the superscript L is used in this side of the interface. At  $t = 0$ , a fluid that is primarily  $H_2$  surrounds the drop and the superscript G is used for  $r > R_d$ . In contrast to the purely subcritical situation [27] where the interface is well defined by a surface where there is a sharp change in density, here there is an arbitrariness in defining an interface that should be followed in time. As we show in the Results section, the gradients of the mass fraction and density do not coincide, so that following the pure drop interface is not equivalent to following the maximum density gradient which is what is optically detected. Since at supercritical conditions the physical phase change interface does not exist, we are free to choose an interface that we want to follow. Ultimately, under subcritical conditions the choice has to be consistent, with the purely subcritical theory.

Since previous results have shown that nonequilibrium effects can be important [24], we do not make the assumption of equilibrium evaporation utilized by all other investigators (c. f. [17], [10] and [14]). The equilibrium evaporation essentially specifies the mass fraction in the gas side once the mass fraction in the drop side and the temperature at the surface are known. The small characteristic time of thermodynamic equilibration introduces another complication in the boundary conditions because it renders the equations very stiff. Nevertheless, nonequilibrium must be considered since there is no physical justification for equilibrium.

Simple accounting of unknowns at the interface yields:  $u_b^L$  and  $u_b^G$ ;  $X_{1b}^L$  and  $X_{1b}^G$ ;  $\rho_b^L$  and  $\rho_b^G$ ;  $R_d$ ;  $\Gamma_b$ ; and  $p_b$ . The interface unknowns are determined from the jump conditions in the conservation of mass density, mass fractions, momentum, and energy; by their very nature, these are computed at

the numerical-cell boundary. The interface variables are related by conservation statements to the variables at adjacent nodes located at numerical-cell centers. Viscous effects are neglected because they are generally very small; so are  $Ma$  effects. Since the pressure is mainly determined by its far field value, the momentum equation at the interface determines only the very small pressure perturbation.

In mathematical form the conservation statements at  $r = R_d$  are:

-mass balance

$$\rho_b^G(u_b^G - dR_d/dt) = \rho_b^L(u_b^L - dR_d/dt) \quad (2.13)$$

We define a mass emission flux,  $F_{ems} \equiv -(1/A_d)dM/dt$  that is consistent with  $F_{ems} = \rho_b^L(u_b^L - dR_d/dt)$ .

-heat balance

$$q_{r,b}^G - q_{r,b}^L = -\{[h_2^G + (h_1^G - h_2^G)X_{1b}^G]/m^G - [h_2^L + (h_1^L - h_2^L)X_{1b}^L]/m^L\}F_{ems} \quad (2.14)$$

where  $h_j^G = h_j(p_b, T_b, X_{1b}^G)$ ,  $h_j^L = h_j(p_b, T_b, X_{1b}^L)$  and  $h_1^G - h_1^L$  is the heat of evaporation whereas  $h_2^G - h_2^L$  is the heat of solution.

- balance of species 1 flux

$$m_1(J_{1r,b}^G - J_{1r,b}^L) = (Y_{1b}^L - Y_{1b}^G)F_{ems} \quad (2.15)$$

-nonequilibrium evaporation law

Calculating the fluxes at the molecular level, one obtains

$$F_{ems} = \sum_{j=1,2} [\alpha_{aj}m_j u_{Tj}(n_{j,equl}^G - n_j^G)] \quad (2.16)$$

where  $n_{j,equl}^G$ 's are calculated from thermodynamic relationships [15] and  $u_{Tj}$  is the mean molecular velocity crossing a plane in one direction. The *expressions* for  $n_{j,equl}^G$ 's are

$$n_{1,equl}^G = [X_{1b}^L \gamma_{1b}^L (\varphi_{1,sat}/\varphi_{1,b}^G) p_{sat,1}(T_b)/(Z^G R_u T_b)] \exp\left(\int_{p_{sat,1}}^{p_b} [v_1^L/(R_u T_b)] dp\right)$$

$$n_{2,equl}^G = \{\rho_b^G X_{2b}^L \gamma_{2b}^L \exp[(\mu_2^{''L} - \mu_2^{''G})/(R_u T_b)]\}/(m^G \gamma_{2b}^G)$$

where  $Z^G = pv/(R_u T)$ .

To calculate the unknowns from the interface jump relationships we proceed as follows:  $u_b^L$  is calculated through the continuity equation in the drop,  $p_b$  is given by the far field value and a perturbation calculated from the momentum equation,  $\rho_b^L$  and  $\rho_b^G$  are calculated from the EOS's once  $T_b$ ,  $X_{1b}^L$  and  $X_{1b}^G$  are known, and  $R_d$  is calculated from the relationship relating it to  $F_{ems}$ . There remains to calculate  $u_b^G$ ,  $F_{ems}$ ,  $X_{1b}^L$ ,  $X_{1b}^G$  and  $T_b$ . That means that we need to calculate five unknowns from four equations; the degree of arbitrariness in choosing the interface location allows to close the system of equations. In our calculations,  $X_{1b}^L$  is specified by the additional use of the species 1 equation in an inner layer at the drop surface. This choice results in  $R_d$  following the regression of the initially pure  $LO_x$ ; in the spatial region where  $r$  is slightly greater  $R_d$ , the mass fraction of  $H_2$  is very small.

## 2.3. Transport properties

### 2.3.1. Viscosities and thermal conductivities

Generic plots of viscosities and thermal conductivities versus  $T/T_c$  are very similar [16]. In the low  $p$  (ideal gas) regime they exhibit an increase with  $T$ , while at high  $p$  they exhibit, a decrease in the low  $T$  regime until a minimum is reached followed by monotonic increase at high  $T/T_c$ . In the high ( $T/TC$ ,  $p/p_c$ ) regime, an asymptotic behavior exists for all curves. This variation suggests a protocol for correlating  $\eta_i(T, p)$  and  $\lambda_i(T, p)$ : first we correlate the values in the low  $p$  limit as a function of  $T$ , then we create an excess function by subtracting the low  $p$  function from the high  $p$  data, and finally we correlate the high  $p$  data versus  $(T, p)$ . The oxygen thermal conductivity obtained through this procedure is depicted in Fig. 1 and shows good agreement with the data represented by the circles.

The individual components properties are used with the corresponding states formalism of Teja and Rice [16] to calculate the mixture properties. his procedure uses averaging with weighing factors which are quantities that are functions of critical properties of each component, Thus

$$\ln[\varepsilon_{mix}^{(\eta)} \eta_{mix}] = \sum_i X_i \ln[\varepsilon_i^{(\eta)} \eta_i], \quad \ln[\varepsilon_{mix}^{(\lambda)} \lambda_{mix}] = \sum_i X_i \ln[\varepsilon_i^{(\lambda)} \lambda_i] \quad (2.17)$$

where  $\varepsilon_i^{(\eta)} = c_\eta v_{ci}^{2/3} / (m_i R_u T_{ci})^{0.5}$  and  $\varepsilon_i^{(\lambda)} = c_\lambda v_{ci}^{2/3} [m_i / (R_u T_{ci})]^{0.5}$  with  $c_\eta$  and  $c_\lambda$  being constants Of value near unity. The values of  $\eta_i$  and  $\lambda_i$  are calculated at  $T_i = T(T_{ci}/T_{c,mix})$  and  $p_i = p(p_{ci}/p_{c,mix})$  where  $T_{c,mix} = \sum_{ij} X_i X_j T_{cij} (v_{cij}/v_{c,mix})$ ,  $T_{cij} = (T_{ci} T_{cj})^{0.5} (1 - k_{ij})$ ,  $v_{cij} = (v_{ci}^{1/3} + v_{cj}^{1/3})^3 / 8$ ,  $v_{c,mix} = \sum_{ij} X_i X_j v_{cij}$ ,  $p_{c,mix} = Z_{c,mix} (R_u T_{c,mix} / v_{c,mix})$ , and  $Z_{c,mix} = \sum_i X_i Z_{ci}$ . The constants  $k_{ij}$  depend on the mixture and are tabulated [16].

To calculate the thermal diffusion factors, we use an expression derived for gases and small  $(m_i - m_j)$  by Hirshfelder et al. [28]

$$\alpha_T^{(ij)} = \epsilon_T (m_i - m_j) / (m_i + m_j) \quad (2.18)$$

where  $\epsilon_T$  is dependent only on  $T$ . According to Bird et al. [29],  $\alpha_T^{(ij)}$  is almost independent of concentration for gases. No formalism for calculating  $\alpha_T^{(ij)}$  for a general fluid exists to our knowledge. In all results presented here  $\epsilon_T$  is taken constant and  $\alpha_T = 0.05$ . Results from calculations with  $\alpha_T$  values of 0.01 and 0.0 at several supercritical pressures are discussed in Harstad and Bellan [23]. Examination of these results shows that they are insensitive to the value of  $\alpha_T$  for the compounds considered and in the range of parameters investigated.

### 2.3.2. Diffusion coefficients

There are four steps in the calculation of the binary diffusion coefficients: First the binary infinite dilution coefficients for a gas are calculated using the formalism of Bird et al. [29]. Second, the infinite dilution coefficients for a liquid are calculated using the formalism of Tyn and Calus [30]. Third, the infinite dilution coefficients for the gas and liquid are combined through an interpolation to yield the infinite dilution coefficients for a binary mixture in both subcritical and supercritical regimes. Fourth, the corresponding states formalism of Teja and Rice [16] is used to calculate the binary diffusion coefficients from the binary infinite dilution coefficients. These formulations are presented briefly below:



1. Infinite dilution coefficients for a gas. According to Bird et al. [29], for a binary mixture where component 1 diffuses into component 2, in the limit  $X_1 \rightarrow 0$ ,

$$D_{12} = \frac{2}{3} \sqrt{\frac{R_u T}{2\pi m_{12}}} \frac{v_2}{N_A Q_{12}} \quad (2.19)$$

where, following corresponding states arguments [29]

$$Q_{12} \simeq l_{c1} l_{c2} (T_R)^{-S(T_R)} \quad (2.20)$$

in which  $T_R = T/\sqrt{T_{c1}T_{c2}}$  and  $l_{cj} \equiv (v_{cj}/N_A)^{1/3}$  characterizes the molecular separation length at the critical point. In the limit  $T_R \ll 1$ ,  $S(T_R) = 0.323$  [29]. The general functional variation of  $S(T_R)$  obtained by fitting experimental data is presented by Reid et al. [16] for  $0.139 < T_R \leq 6.2$ ; the curve is here fitted by  $S(T_R) = 0.426 - 0.1741 \ln T_R - 0.04656(111 - T_R)^2 + 0.03447(\ln T_R)^3$ . For  $T_R < 0.139$ ,  $S(T_R) = 0.3234$  is used, whereas for  $T_R > 6.2$ ,  $S(T_R) = 0.16272$  (which is the value at  $T_R = 6.2$ ) is used.

2. Infinite dilution coefficients for a liquid. The Stokes-Einstein formula calculates the mobility of a molecule assuming that it behaves as a sphere in a slow flow, and thus that its motion can be described by the combined effect of inertia and Stokes drag. The result is that the molecule appears to diffuse through the flow with an effective diffusion coefficient that is related to the medium viscosity. If one imagines this molecule belonging to component 1 and the *medium* being the pure component 2, one obtains the infinite dilution diffusion coefficient for liquids

$$D_{12} = \frac{R_u T}{N_A \eta_2 l'_1} \quad (2.21)$$

where the characteristic molecular scale length is  $l'_1 = 4\pi d_1$ . The Eyring theory combined with data correlating an activation energy to the latent heat of evaporation provides the means to calculate the viscosity  $\eta_2$  [28]. In Eyring's theory, an activated state is defined as that having the longest characteristic time for a process; in the context of molecular motion, it is the time necessary for a molecule to jump from one site to another assuming that the liquid has a lattice-like structure. Since the bonds between molecules are also those necessary to break during evaporation, it is natural to relate the free energy of activation to the enthalpy of evaporation (see Bird et al. [29]). The combined result is

$$\eta_2 \simeq \frac{l_2 \sqrt{2\pi m_2 R_u T}}{v_2} \exp[G_2/(R_u T)] \quad (2.22)$$

where  $G_2 \equiv \Delta G_2 - R_u T \ln[l_2 \sqrt{2\pi m_2 R_u T}/(h_p N_A)]$ ,  $\Delta G_2 = 0.408(\Delta h_{2, \text{evap}} - R_u T)$  evaluated at  $T = T_{2, \text{nb}}$ , and  $l_2 = (v_2/N_A)^{1/3}$ . The value of  $d_1$  is provided by the Tyn and Calus formula [30], [16] based on the theory of corresponding states; in microns, the result is

$$d_1 = 1.23 \times 10^{-4} \left( \frac{\sigma_{1, \text{nb}}}{\sigma_{2, \text{nb}}} \right)^{0.15} \left( \frac{v_{1, \text{nb}}^{0.433}}{v_{2, \text{nb}}^{0.267}} \right) \quad (2.23)$$

3. Infinite dilution diffusion coefficient for a fluid. The forms of Eqs. 2.19 and 2.20 for a gas, and the combination of Eqs. 2.21, 2.22, 2.23 yielding  $D_{12}$  suggest the form of the expression for a general fluid:

$$D_{12} = u_{T2}(l_2^2/l_1')f_{12} \quad (2.24)$$

where  $f_{12}$  is an extension function from the gas to the liquid behavior. From the results of Bird et al. [29], it may be inferred that for a liquid

$$u_{T2} = \sqrt{\frac{R_u T}{2\pi m_2}} \exp[-G_2/(R_u T)] \quad (2.25)$$

where  $G_2$  is positive. For a gas, the same formula applies with  $G_2 \equiv 0$ . Both behaviors are captured by replacing  $G_2$  by  $\max(G_2, 0)$  in Eq. 2.25. Function  $f_{12}$  is chosen to insure that the gas and liquid expressions for  $D_{12}$  are recovered; since  $f_{12}^{(liq)} = 1$ , whereas  $f_{12}^{(gas)} \gg 1$  because both  $v_2$  and  $l_2$  are large, an interpolation between gas and liquid values is appropriate. Thus

$$\begin{aligned} f_{12}^{(gas)} &= \frac{2}{3} \sqrt{1 + \frac{m_2}{m_1}} \left( \frac{l_1' l_2}{l_{c1} l_{c2}} \right) T_R^{S(T_R)} \\ f_{12}^{(fluid)} &= \max(1, f_{12}^{(gas)}) \\ f_{12}^{(liq)} &= 1 \end{aligned}$$

Errors of 10%-30% or more may be expected in the fluid regime. However, no practical theory that is better for calculating infinite dilution diffusion coefficients for a general fluid is available.

4. Mixture binary diffusion coefficients for a general binary fluid. The corresponding states formalism used by Teja and Rice [16] for calculating diffusion coefficients yields

$$\ln[\varepsilon_{mix}^{(D)} D_{mix}] = X_1 \ln[\varepsilon_1^{(D)} D_{21}] + X_2 \ln[\varepsilon_2^{(D)} D_{12}] \quad (2.26)$$

where  $\varepsilon_j^{(D)} \equiv v_{cj}^{-1/3} \sqrt{m_j/(R_u T_{cj})}$ . Equation 2.26 is the final expression for binary diffusion coefficients for a general binary fluid. An example of the calculation using 2.26 appears in Fig. 2.

### 3. Numerical method

As mentioned above,  $Ma \ll 1$ , and thus the pressure is calculated as  $p(r, t) = p_m(t) + p'(r, t)$  where  $p_m(t)$  is specified and  $p'(r, t)$  is a small perturbation calculated from the momentum equation.

The equations are recast in a convenient form for numerical analysis as follows: The density derivatives in Eq. 2.1 are replaced using the relationship

$$d(1/\rho) = -\alpha_v dT + \kappa_T dp + \sum_1^N (m_j/m - v_j/v) dX_j \quad (3.1)$$

where  $\kappa_T = -(1/v)(\partial v/\partial p)_T$ ,  $X_j$  is the isothermal compressibility. Combining Eq. 3.1, 2.1, 2.10 and 2.11 yields

$$\nabla \cdot \vec{u} = -\frac{D \ln \rho}{Dt} = \nu_\rho - \kappa_s \left( \frac{dp_\infty}{dt} + \frac{Dp'}{Dt} \right) \quad (3.2)$$

where the dissipative expansion

$$\nu_\rho = \frac{\alpha_v}{nC_p} (\Phi_v - \nabla \cdot \vec{q}) + \sum_1^N \left( \frac{\alpha_v}{nC_p} h_j - v_j \right) \nabla \cdot \vec{J}_j \quad (3.3)$$

represents the effect of entropy production and  $\kappa_s = \kappa_T - (\alpha_v)^2 T / (n C_p)$  is the isentropic compressibility.

The primitive variables are  $p$ ,  $T$ ,  $X_j$  (or  $Y_j$ ), and  $u_\beta$ . The quantities  $\rho$ ,  $\alpha_D$ ,  $C_p$ ,  $\alpha_v$ ,  $\kappa_s$ ,  $v_j$  and  $h_j$  are calculated from the state equation. At any time step, the solution is found by iterating in two sequential pairs. The first pair is  $u_r$  and  $p$ ; the second pair is  $T$  and  $Y_1$ . Spherical symmetry is assumed and the  $r$  coordinate is given by a time dependent, grid. The thermodynamic variables are calculated at grid cell centers, whereas the velocity and fluxes are calculated at grid cell boundaries. The grid motion is determined by fixing one boundary at the moving interface,  $R_d(t)$ , and by choosing the outermost boundary,  $R_{si}(t)$ , to follow the fluid motion (Lagrangian far field boundary);  $dR_{si}/dt = u_r(r = R_{si})$ . Due to expected sharp gradients, the grid spacing is smallest near the interface.

An iterate of the flow dynamics ( $u_r, p$ ) pair is done in two steps. First, Eq. 3.2 is used to produce a predicted velocity when  $p$  is neglected and the small viscous dissipation is estimated by the prior iterate; the interface velocity jump is applied. Second, Eqs. 2.2 and 3.2 are used to correct the velocity and find  $p$  through the use of a potential function.

The second pair of variables,  $(T, Y_1)$  is obtained by iteratively solving Eqs. 2.10 and 2.11 as a pair of coupled convection-diffusion equations. Upwind differencing of the convection terms is used in regions of large gradients; relative to the local grid motion, the effective convection velocity is  $u_r - dr_g/dt$ . The difference equations for the time dependent vectors of cell center values of  $T$  and  $Y_1$  are in the form of coupled matrix equations. The matrix elements related to cells at the interface are modified to satisfy the conditions at the interface. At the chop center, the gradients are null; at the far field boundary, the values of the variables are known. During any particular time step, an iterate is accomplished by a two stage process: first, there is a partial explicit time step which is followed by an implicit time step. The implicit, time step requires a matrix iteration based on the Thomas algorithm for inverting tridiagonal matrices [31].

Because the time constant, associated with Eq. 2.16 is very small, the equations are very stiff. Therefore, during a time step iterate, a separate iteration is required to calculate the interface conditions. These conditions are then used in the radial velocity calculations and in the formation of the  $(T, Y_1)$  vector pair matrices.

## 4. Results

In order to better understand the trends predicted by this model, we first analyze a baseline calculation and then present a parametric study.

### 4.1. Baseline behavior

The initial conditions for the calculation are:  $R_d^0 = 50 \times 10^{-4}$  cm,  $R_{si} = 0.1$  cm,  $T_{d,b}^0 = -100$  K (the fluid drop temperature is assumed initially uniform),  $T_{si}^0 = 1000$  K,  $p = 20$  MPa. The fluid drop is composed of pure  $LO_r$  ( $T_c = 154.6$  K,  $p_c = 5.043$  MPa), while the surrounding is hydrogen ( $T_c = 33.2$  K,  $p_c = 1.313$  MPa); in order to avoid an initial discontinuity that violates jump conditions, a small amount of oxygen exists initially in the drop surroundings, its distribution vanishing with increasing  $r$ . Since these initial conditions are in the supercritical  $LO_r$  regime, evaporation does not occur and the traditional concept of drop lifetime is meaningless. Therefore, the results are presented in terms

of variation of the dependent variables over the entire spatial domain without reference to any interface.

Figure 3 illustrates the spatial variation of  $T$ ,  $p$  and  $Y_1$  ( $i = 1$  refers to  $LO_x$ ) as a function of time. Comparisons between the variation of these quantities shows that the density gradient is the steepest, however it does not remain steep during the entire time necessary for chop heating. It is this density gradient that is captured in optical measurements such as Gökalp's [19]; since the gradient eventually relaxes, the optical measurement yields increasingly uncertain results as  $t$  increases. The density gradient does not correspond to the  $Y_1$  gradient indicating that it is not the evolution of the pure  $LO_x$  fluid drop that is followed in the measurements, but that of an entity into which hydrogen has diffused. The pure  $LO_x$  fluid drop shrinks very fast and eventually disappears as shown in Fig. 3 by  $Y_1(r = 0) < 1$ . It is important, to realize that not only do gradients of  $Y_1$  and  $T$  occur at different locations, but also that early-time gradients of  $T$  are steeper than gradients of  $Y_1$  whereas at later time the opposite is true. In fact, relaxation of the  $T$  and  $\rho$  profiles occurs much faster than that of  $Y_1$  as seen in the very long time behavior illustrated in Fig. 4. This is because  $D_T$  is considerably larger than  $D_m$  as shown by their ratio, the traditional  $Le$  plotted in Fig. 5. However, while under subcritical conditions  $Le$  is the ratio of heat to mass fluxes, under supercritical conditions  $Le$  is a misleading measure of the flux ratio [23]. On Fig. 5, an effective Lewis number,  $Le_{eff}$ , based upon a boundary layer, quasi-steady estimate of the thermal and mass diffusion length scales [23] is illustrated as well. Comparison of  $Le$  versus  $Le_{eff}$  shows that the effective Lewis number is about a factor of 40 larger than the traditional  $Le$ . The traditional  $Le$  is calculated under the assumption that the molar flux is proportional to mass fraction gradients and the heat flux is proportional to temperature gradients, an assumption that is not satisfied in the present situation. Comparisons between our results and those of Yang et al. [10] for  $Le$  shows that we predict similar  $Le$  variations, although our values are larger for a given pressure, as will be discussed in the parametric variations Mow.

Properties related to heat transfer are depicted in Fig. 6:  $C_p$  is larger in the fluid drop whereas  $\lambda$  is larger in the drop surroundings. This means that it is more difficult to heat the drop than the drop surroundings ( $C_p$  is larger in the chop), and that heat is more difficult to transmit inside the drop than in its surroundings ( $\lambda$  is larger in the drop surroundings than in the chop). Our plots for  $\lambda$  show a wider scale variation than those of Yang et al. [10] for same  $R_d^0$  and  $T_{si}^0$  but larger  $p$  at similar times. As will be seen below, the scales become smaller (i. e. gradients become larger) with increasing pressure and thus our results quantitatively disagree with the small scales shown by Yang et al. [10] at approximately 12.5 MPa (a pressure smaller than that of 20 MPa as in our calculations). It is speculated that the discrepancy comes from our inclusion of additional terms [23] in the model and calculations.

$Y_1$  versus  $T$  is displayed in Fig. 7 as a function of time in order to parallel previous plots by other authors [17] for very similar supercritical conditions; the only differences are their initial radius of  $100 \times 10^{-4}$  cm and  $p = 8$  MPa. Our results show none of the discontinuities displayed by the results of Haldenwang et al. [17] which appeared as a consequence of their equilibrium assumption. The plots in Fig. 7 resemble in shape those of Delplanque and Sirignano [14] obtained also at supercritical conditions ( $p = 10.086$  MPa,  $T_\infty = 1500$  K) for a burning droplet of identical initial size, although their plots are restricted to a droplet interior whose definition is not given (the criterion for the interface location under supercritical conditions is missing). The small deviation of among all curves on Fig. 7 for such a wide time interval suggests almost a similarity solution; this is an unexpected result given the complexity of the equations.  $\rho$  versus  $T$  is plotted in Fig. 8

as a function of  $t$ ; away from the initial condition all the plots fall on the same line pointing again to a similarity solution. These plots are for a larger temperatures than those of Yang et al. [10] but for a similar pressure regime. Comparisons with those plots are not possible since those results were obtained from phase equilibrium calculations for a liquid mixture of  $LO_x$  and  $H_2$ .

To evaluate the assumption of constant  $\rho D_m$  made by other authors [14], we show in Fig. 9 spatial plots of this quantity at different times. The plots show that the initially uniform profiles in each side of the interface evolve strong nonuniformities with time; thus the assumption of constant  $\rho D_m$  should be discarded from all supercritical regime studies.

## 4.2. Parametric study

The variation of the above results with initial fluid-drop size, surrounding pressure and surrounding temperature is important, for coaxial atomizer design. To explore the impact of these variations, the results of the parametric study are discussed below.

### 4.2.1. Influence of initial fluid-drop size

To examine the impact of the initial size, calculations were performed with drops of initial radius  $25 \times 10^{-4}$  cm and  $300 \times 10^{-4}$  cm and compared to those of the baseline case; plots of the results at  $5 \times 10^{-3}$  s appear in Fig. 10. The main result of increasing the drop size is to delay drop heating, produce a more uniform  $LO_x$  distribution at this time, and maintain the strong density gradient, for longer times. Since optical measurements of the interface location correspond to the density gradient, it is expected that experimental information on the interface motion will be more accurate for larger drops.

### 4.2.2. Influence of surrounding pressure

in Figs. 11 and 12 we display results for fixed initial drop size and surrounding temperature as a function of surrounding pressure at  $2 \times 10^{-2}$  s. The almost, constant,  $\lambda$  but much larger  $C_p$  with increasing  $p$  on the  $LO_x$  side of the interface (not shown) result in smaller  $T'$  on the  $LO_x$  side of the interface; the opposite occurs on the  $H_2$  side of the interface. Thus,  $T$  gradients are greater with increasing  $p$ . Increasing the surrounding  $p$  decreases both  $D_m$  and  $D_T$  (not shown); however, there is relatively a larger reduction on the  $H_2$  side of the interface. The decrease in  $D_m$  explains the smaller  $Y_1$  on the  $H_2$  side of the interface and the steeper gradients with increasing  $p$ . Examination of the  $\rho$  profiles shows the considerably larger gradients with increasing  $p$ ; it is thus inferred that experiments quantifying the interface motion will be more accurate when performed at large pressures. Figure 12 illustrates the spatial variation of  $\rho D_m$  at different  $p$  and **confirms** that the assumption of constant  $\rho D_m$  deteriorates with increasing  $p$ . This is an expected result since the classical evaluation of  $D_m$  as a function of  $T'$  that is the basis of this assumption is strictly valid only in the limit of the low  $p$  (gas) regime.

Examination of the variation of  $Le$  with increasing  $p$  [23] shows that as  $p$  increases,  $Le$  remains  $< 1$  on the  $LO_x$  side of the interface, and decreases with increasing  $p$ , whereas  $Le$  remains  $> 1$  on the  $H_2$  side of the interface and increases with increasing  $p$  [23]. This spatial variation with increasing  $p$  shows that indeed the gradients become steeper with increasing  $p$ . The Lewis number seems insensitive to the pressure in the far field.

The general variation of the dependent variables with increasing  $p$  indicates that since the gradients become larger due to a reduction in scales, high pressure combustion in practical devices will have to rely on strong turbulence to enhance mixing and heat transfer.

#### 4.2.3. Influence of surrounding temperature

Figure 13 contains plots illustrating results at  $2 \times 10^{-2}$  s from calculations at  $T_{si}^0 = 1000$  K and 500 K for  $p = 20, 40$  and  $80$  MPa. Spatial plots of the transport properties (not illustrated) show that  $D_m, D_T$  and  $\lambda$  all increase with increasing  $T_{si}^0$ , however,  $Le$  decreases with increasing  $T_{si}^0$  on the  $H_2$  side immediately adjacent to the interface before the asymptotic increasing trend reappears [23]. On the  $LO_x$  side of the interface,  $Le$  remains  $< 1$  and increases with increasing  $T_{si}^0$ , however, the difference becomes smaller with increasing  $p$  [23]; on the  $H_2$  side of the interface  $Le$  remains  $> 1$  [23]. This means that scales become smaller with decreasing  $T_{si}^0$ , an effect immediately apparent upon examination of the  $\rho$  profiles. The larger gradients at smaller  $T_{si}^0$  imply that experiments with drops at lower  $T_{si}^0$  will yield data carrying less uncertainty about the interface motion since it would be more easily detectable.

As expected from the variation of  $D_m$ , diffusion of  $LO_x$  is enhanced at larger temperatures but the difference decreases with increasing pressure, a result easily observable in Fig. 13. The  $T$  plots depicted in Fig. 13 show the same trends regarding the relative gradients magnitude as those found in the plots of  $\rho$  and  $Y_i$ . The larger  $T$  on the  $LO_x$  side of the interface with decreasing pressure at the larger  $T_{si}^0$  and the smaller  $T$  with decreasing pressure at the smaller  $T_{si}^0$  are the effect of the larger reduction of  $LO_x$  at those locations at the larger  $T_{si}^0$ ; in fact the variation at smaller  $T_{si}^0$  is a snapshot of the early behavior of the drop at larger  $T_{si}^0$ .

## 5. Conclusions

A model of an isolated fluid drop in quiescent, finite spatial surroundings has been derived using the formalism of fluctuation theory. The model presented here is derived from first principles and incorporates all physical aspects of high pressure behavior including Soret and Dufour effects, high pressure mixture-thermodynamics and mixture transport properties over a wide range of pressures and temperatures.

Results obtained for the  $LO_x - H_2$  system show that the supercritical behavior is that of a slow diffusion process. The spatial temperature profile is the first to relax, followed by the density profile; the mass fractions remain nonuniform long after relaxation of both temperature and density. Given the long characteristic time associated with diffusion, it is not surprising that strong turbulence is needed to mix  $LO_x$  and  $H_2$  in liquid rocket motors. The results are insensitive to the variation of the thermal diffusion factor (within the range 0.0-0.05 and up to 80 MPa) when this factor is assumed constant with time and uniform [23]. This is remarkable considering that the thermal diffusion factor is the only free parameter in the present calculations. Also unexpected is the self-similar behavior of the  $LO_x$  mass fraction versus the temperature obtained by eliminating the radial variation between the two dependent variables.

An important, although not unexpected finding is that the uniformity assumption for the product of the density by the mass diffusivity is not justified. Additionally, consistent with the different, relaxation times of the temperature and mass fractions, the traditional Lewis number is shown to

be much smaller than an effective Lewis number estimated from a quasi-steady, boundary layer theory presented elsewhere [23].

Parametric studies performed by varying the initial fluid-drop size, the surrounding pressure and the surrounding temperature show that gradients become larger with increasing pressure and smaller temperatures. The practical consequence of this finding is that increasing turbulence is necessary to mix the reactants at larger pressures.

The above results could not be experimentally validated due to lack of observation of free fluid drops in supercritical, quiescent surroundings. Our results show that optical experimental data must be interpreted with caution since the detected density gradients are maintained only for limited times. In that respect, the most accurate data is expected for large drops in high pressure and low temperature surroundings because the density gradients survive longer with increasing fluid-drop size and pressure, and with decreasing temperature.

#### ACKNOWLEDGMENT

This research was conducted at the Jet Propulsion Laboratory under sponsorship from the National Aeronautics and Space Administration, the George C. Marshall Space Flight Center with Mr. Klaus W. Gross as technical contract, monitor. His continuing interest, and support are greatly appreciated.

## References

- [1] Harrje, D. T. and Reardon, F. H., *Liquid Propellant Rocket Combustion Instability*, NASA SP-194 (1972)
- [2] Williams, F. A., *Combustion Theory*, Addison-Wesley (1965)
- [3] Chervinsky, A., Transient burning of spherical symmetric fuel droplets, *Isr. J. Technol.* **7**, 66-73 (1969)
- [4] Nuruzzaman, A. S. M. and Beer, J. M., On the nonsteady nature of droplet combustion, *Combust. Sci. and Tech.* **3**, 17-24 (1971)
- [5] Matlosz, R. L., Leipziger, S. and Torda, T. I., Investigation of a liquid drop evaporation in a high temperature and high pressure environment, *Int. J. Heat Mass Transfer* **15**, 831-852 (1972)
- [6] Rosner, D. E. and Chang, W. S., Transient evaporation and combustion of a fuel droplet near its critical temperature, *Combust. Sci. and Tech.* **7**, 145-158 (1973)
- [7] Crespo, A. and Linan, A., Unsteady effects in droplet evaporation and combustion, *Combust. Sci. and Tech.* **11**, 9-18 (1975)
- [8] Chesneau, X., Chauveau, C. and Gökalp, I., Experiments of high pressure vaporization of liquid oxygen droplets, AIAA 94-0688, 32nd Aerospace Sciences Meeting, Reno, NV (1994)
- [9] Givler, S. D. and Abraham, J., Supercritical droplet, vaporization and combustion studies, *Prog. Energy Combust. Sci.*, **22**, 1-28 (1996)
- [10] Yang, V., Lin, N. and Shuen, J-S., Vaporization of liquid oxygen (LOX) droplets in supercritical hydrogen environments, *Combust. Sci. and Tech.*, **97**, 247-270, 1994
- [11] Scheibel, E. G., Liquid diffusivities, *Industrial Engineering Chemistry*, **46**, 2007-2008 (1954)
- [12] Takahashi, S., Preparation of a generalized chart for diffusion coefficients of gases at high pressures, *Journal of Chemical Engineering (Japan)*, **7**, 417-420 (1974)
- [13] Hsiao, G. C., Yang V. and Shuen, J. S., Supercritical vaporization and dynamics of liquid oxygen (LOX) droplet in hydrogen stream, AIAA 95-0383, 33rd Aerospace Sciences Meeting, Reno, NV (1995)
- [14] Delplanque, J-P. and Sirignano, W. A., Numerical study of the transient vaporization of an oxygen droplet at sub- and super-critical conditions, *Int. J. Heat Mass Transfer*, **36**(2), 303-314 (1993)
- [15] Prausnitz, J., Lichtenthaler, R. and de Azevedo, E., *Molecular thermodynamics for fluid-phase equilibrium*, Prentice -Hall, Inc. (1986)



- [16] Reid, R. C., Prausnitz, J. M. and Polling, B. E., The Properties of Gases and Liquids, 4th Edition, McGraw-Hill Book Company, 1987
- [17] Haldenwang, P., Nicoli, C. and Daou, J., High pressure vaporization of LOX droplet crossing the critical condition, *Int. J. Heat Mass Transfer*, 39(16), 3453-3464 (1996)
- [18] Sate, J., Tsue, M., Niwa, M. and Kono, M., Effects of natural convection on high-pressure droplet combustion, *Combust. and Flame*, 82, 142-150 (1990)
- [19] Chauveau, C. and Gökalp, I., Experiments on the vaporization of  $\text{LO}_x$  droplets under high pressure, submitted (1997)
- [20] Chauveau, C., Chesnau, X. and Gökalp, I., Burning characteristics of n-heptane droplets, AIAA 93-0824, 31st Aerospace Sciences Meeting, Reno, NV. (1993)
- [21] Chauveau, C., Chesnau, X. and Gökalp, I., High pressure vaporization and burning of methanol droplets in reduced gravity, AIAA 94-0430, 32nd Aerospace Sciences Meeting, Reno, NV. (1994)
- [22] Harstad, K. G., Miller, R. S., and Bellan, J., Efficient High Pressure State Equations, accepted for publication, *A. I. Ch. E.*, 1997
- [23] Harstad, K. and Bellan, J., The Lewis number under supercritical conditions, submitted (1997)
- [24] Bellan, J. and Summerfield, M., Theoretical examination of assumptions commonly used for the gas phase surrounding a burning droplet, *Combust. and Flame*, 33, 107-122 (1978)
- [25] Keizer, J., Statistical Thermodynamics of Nonequilibrium Processes, Springer-Verlag, New York, 1987
- [26] Peacock-Lopez, E. and Woodhouse, L., Generalized transport, theory and its application to binary mixtures, *Fluctuation Theory of Mixtures*, Advances in thermodynamics, Vol. 2, Eds. Matteoli, E. and Mansoori, G. A., Taylor and Francis, 301-333, 1983
- [27] Bellan, J. and Cuffel, R., A theory of non-dilute spray evaporation based upon multiple drop interaction, *Combust. and Flame*, 51, No. 1, 55-67 (1983)
- [28] Hirshfelder, J. O., Curtis, C. F. and Bird, R. B., *Molecular Theory of Gases and Liquids*, John Wiley and Sons, Inc. (1964)
- [29] Bird, R. B., Stewart, W. E. and Lightfoot, E. N., *Transport Phenomena*, John Wiley and Sons, 1960
- [30] Tyn, M. T. and Calus, W. F., Diffusion coefficients in dilute binary mixtures, *J. of Chem. Eng. Data*, 20(1), 106-109 (1975)
- [31] Anderson, D. A., Tannehill, J. C. and Pletcher, R. H., *Computational Fluid Mechanics and Heat Transfer*, Hemisphere Publ. Corp., N. Y., 1984

## NOMENCLATURE

$A_d$	fluid drop surface area
$C_p$	molar heat capacity at constant pressure
$d$	characteristic molecular interaction length
$D$	diffusion coefficients
$F_{ems}$	emission flux
$G$	Gibbs free energy
$h$	molar enthalpy
$h_p$	Planck's constant,
$J$	molar flux
$k$	set of tabulated constants for two species
$l$	molecular separation length
$l'$	characteristic molecular length scale
$L$	transport matrix
$L_{ij}$	elements of the transport matrix $L$
$Le$	Lewis number
$m$	molar mass
$\bar{m}$	reduced molar mass
$M$	fluid drop mass
$Ma$	Mach number
$n$	number of moles per unit volume
$N$	number of species
$N_A$	Avogadro's number
$p$	pressure
$q$	heat flux
$Q$	collision cross section
$r$	radial coordinate
$R_d$	drop radius
$R_u$	universal gas constant,
$t$	time
$T$	temperature
$u$	velocity
$u_T$	mean, normal velocity of a molecule due to thermal fluctuations
$v$	molar volume
$x$	generic coordinate
$X$	mole fraction
$Y$	mass fraction
$Z$	compressibility factor

GREEK

$\alpha_a$	accomodation coefficients
$\alpha_D$	mass diffusion factors
$\alpha_T$	thermal diffusion factor
$\alpha_v$	thermal expansion ratio
$\beta$	$1/(RT')$
$\gamma$	activity coefficient
$\Delta G$	free energy of activation in Eyring's theory
$\Delta h$	latent heat
$\eta$	viscosity
$\kappa_s$	isentropic compressibility
$\kappa_T$	isothermal compressibility
$\lambda$	thermal conductivity
$\mu$	chemical potential
$\nu_\rho$	dissipative expansion
$\rho$	density
$\sigma$	surface tension
$\tau$	stress tensor
$\Phi_v$	viscous dissipation
$\varphi$	gas fugacity coefficient

## SUBSCRIPTS

$\alpha, \beta$	coordinate notation
$b$	drop interface, at $r = R_d$
$c$	critical point property
$d$	drop
$eff$	effective
$equil$	thermodynamic equilibrium
$evap$	evaporation
$g$	grid
$i, j$	species
$m$	mass
$mix$	mixture
$nb$	normal boiling point
$r$	radial component
$sat$	saturation
$si$	at the edge of the sphere of influence
$T'$	thermal
$\infty$	far field

## SUPERSCRIPTS

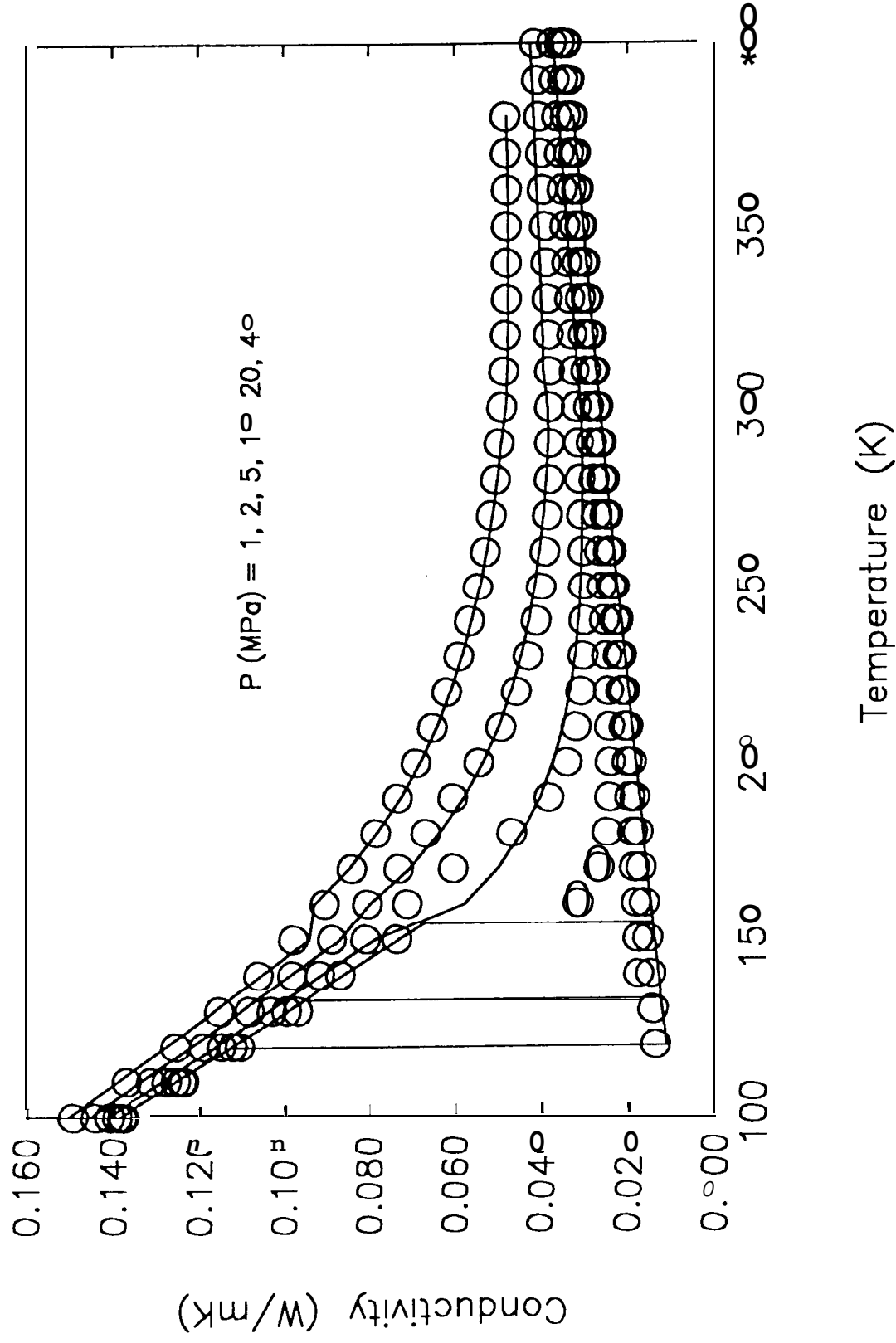
<i>gas</i>	gas
<i>G</i>	<i>on</i> the initial hydrogen side
<i>fluid</i>	fluid
<i>i, j</i>	species
<i>liq</i>	liquid
<i>L</i>	<b>on the</b> initial oxygen side
<i>0</i>	initial value
<i>"</i>	pure substance

## FIGURE CAPTIONS

- Fig. 1** Fitted values of the oxygen thermal conductivity and comparison with experimental data.
- Fig. 2** Calculation of the mass diffusion coefficient for an equimolar mixture of hydrogen and oxygen
- Fig. 3** **Spatial variation of the temperature, oxygen mass fraction and density** at various times for  $R_d^0 = 50 \times 10^{-4}$  cm,  $R_{si} = 0.1$  cm,  $T_{d,b}^0 = 100$  K,  $T_{si}^0 = 1000$  K, and  $p = 20$  MPa. The curves correspond to the following times: 0.0 s (---),  $7.5 \times 10^{-3}$  s (- - -),  $1.25 \times 10^{-2}$  s (- · - · -),  $1.5 \times 10^{-2}$  s ( “ “ “ “ ),  $1.75 \times 10^{-2}$  s ( -- “ - ),  $2.414 \times 10^{-2}$  S ( - · · - ).
- Fig. 4** Long time behavior of the oxygen mass fraction for the initial conditions in the Fig.3 caption. The curves correspond to the following times: 0.0 s (----),  $5 \times 10^{-2}$  S (- - -),  $1 \times 10^{-1}$  s (- · - · -),  $1.5 \times 10^{-1}$  s (····),  $1.763 \times 10^{-1}$  s ( - · · - ).
- Fig. 5** Spatial variation of the traditional and an effective Lewis number at different times. The initial conditions are those of Fig. 3 caption.
- Fig. 6** Spatial variation of  $C_p$  and  $\lambda$  for the initial conditions in Fig. 3 caption. Curves are labeled as in Fig.3 caption.
- Fig. 7** Temporal variation of the oxygen mass fraction versus the temperature for the initial conditions in Fig.3 caption. The curves are labeled as in Fig. 3 caption.
- Fig. 8** Temporal variation of the density versus the temperature for the initial conditions in Fig.3 caption. The curves are labeled as in Fig. 3 caption.
- Fig. 9** Spatial variation of  $\rho D_m$  for the initial condition in Fig.3 caption. The curves are labeled as in Fig.3 caption.
- Fig. 10** Spatial variation of the temperature, oxygen mass fraction and density at 25 MPa. Plots are at  $5 \times 10^{-3}$  s for initial fluid drop radii  $25 \times 10^{-4}$  cm (— · — · —),  $50 \times 10^{-4}$  cm (- · - · -) and  $300 \times 10^{-4}$  cm (· · · · ·).
- Fig. 11** Spatial variation of the temperature, oxygen mass fraction and density at  $2 \times 10^{-2}$  s for several pressures: 10 MPa (- - -), 20 MPa (- · - · -), 25 MPa (· · · · ·), 40 MPa (- - -), 80 MPa (- · · · -). Other initial conditions are:  $R_d^0 = 50 \times 10^{-4}$  cm,  $R_{si} = 0.1$  cm,  $T_{d,b}^0 = 100$  K,  $T_{si}^0 = 1000$  K.
- Fig. 12** Spatial variation of  $\rho D_m$  for the initial condition in Fig. 11 caption. The curves are labeled as in Fig. 11 caption.
- Fig. 13** Spatial variation of the temperature, oxygen mass fraction and density at  $T_{si}^0 = 1000$  K (—), (— · —) and (— · · · —); and at  $T_{si}^0 = 500$  K (····), (— · —) and (— · · —). The other initial conditions are:  $R_d^0 = 50 \times 10^{-4}$  cm,  $R_{si} = 0.1$  cm, and  $T_{d,b}^0 = 100$  K. Results are at  $2 \times 10^{-2}$  s and for several pressures: 20 MPa (---) and (····); 40 MPa (- - -) and (- · -); and 80 MPa (- · - · -) and (- · · -).

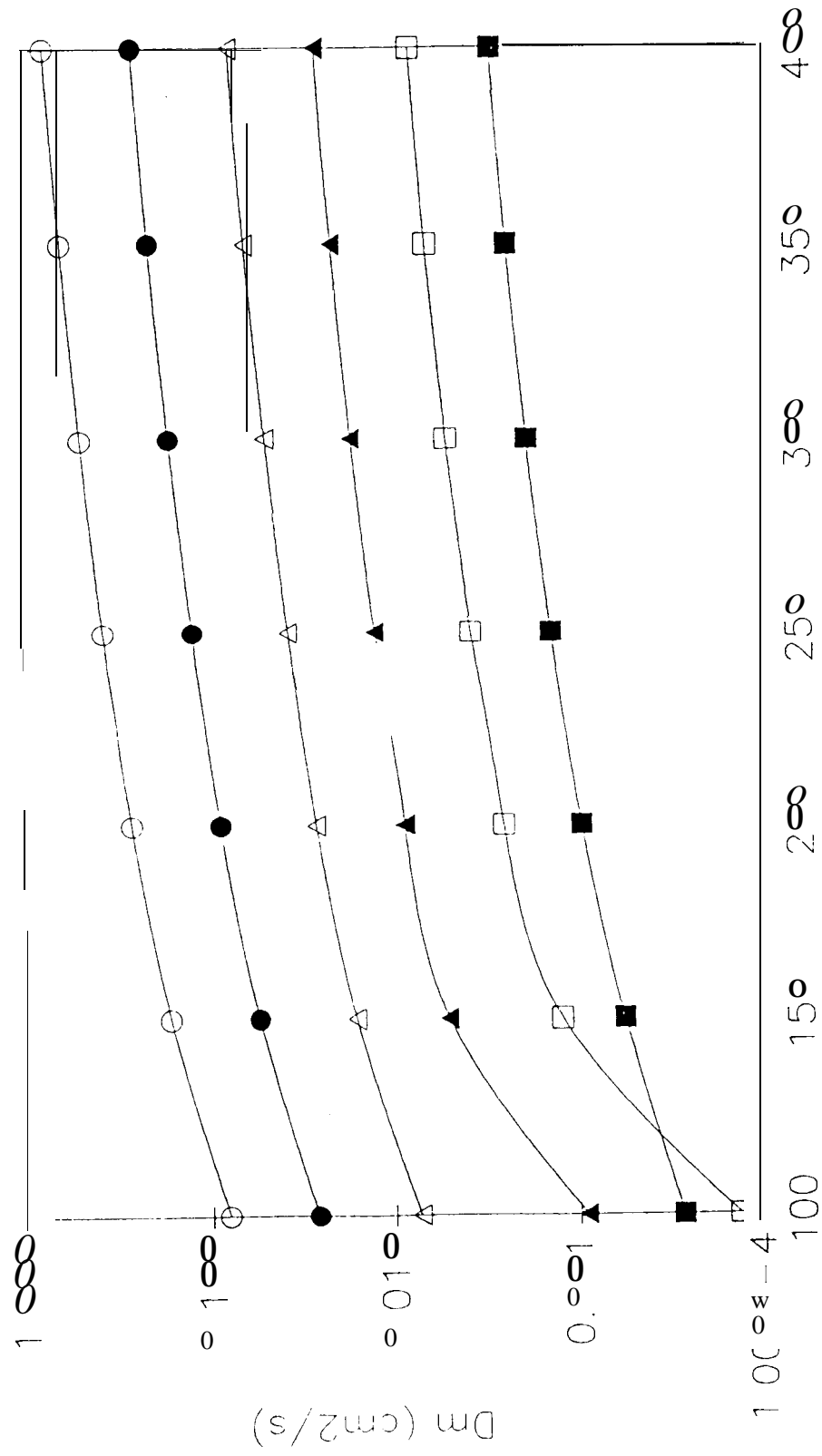
# Thermal Conductivity of Oxygen

(Circles denote fitted data)



# Mass Diffusion Coefficient - Equimolar H<sub>2</sub> and O<sub>2</sub>

$\circ$  —  $p = 0.1$      $\bullet$  —  $p = 0.3$      $\Delta$  —  $p = .0$   
 $\square$  —  $p = 1.0$      $\blacksquare$  —  $p = 3.0$



Temperature (K)

Fig 2

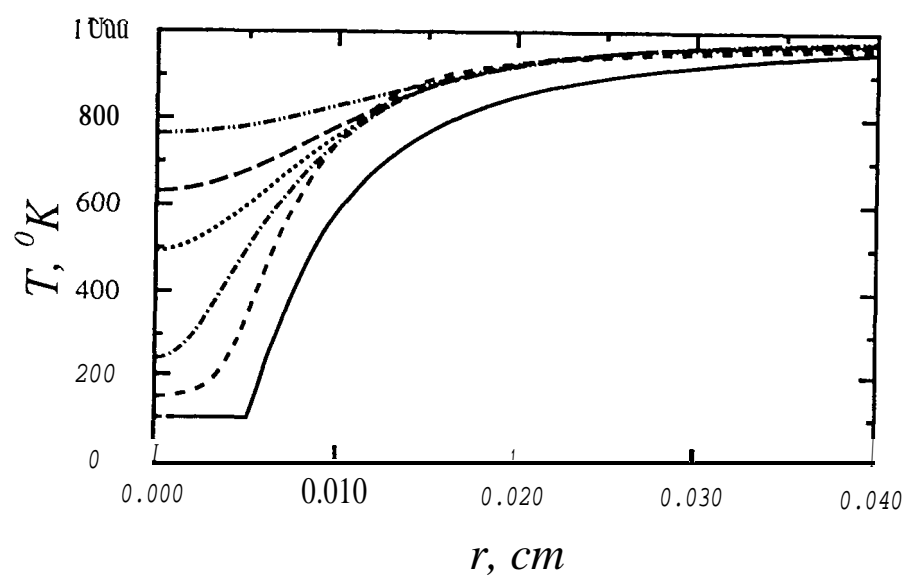
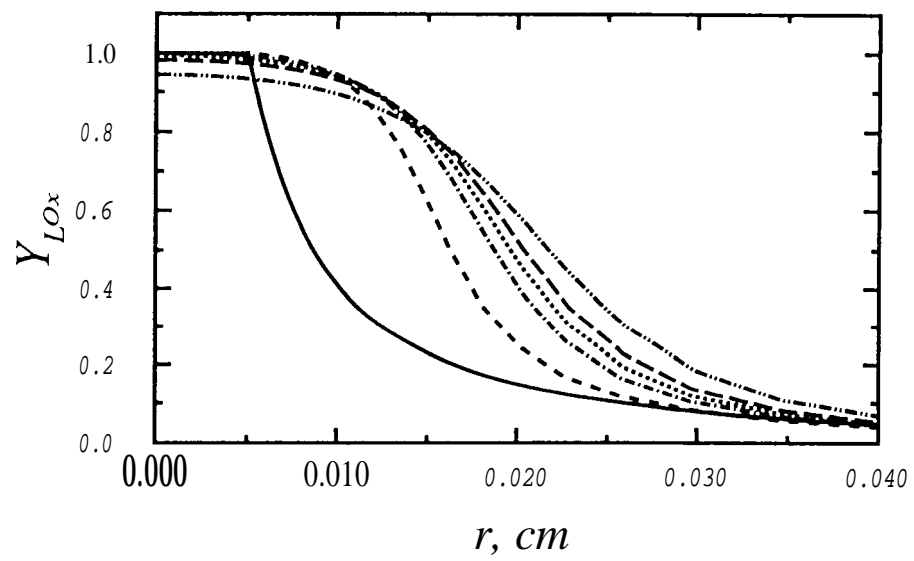


Fig 3a





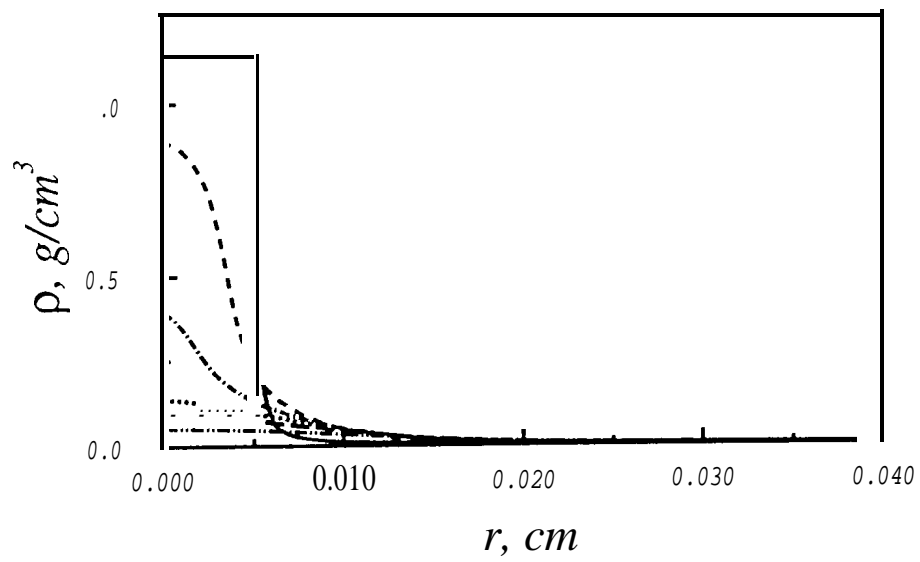


Fig 3c

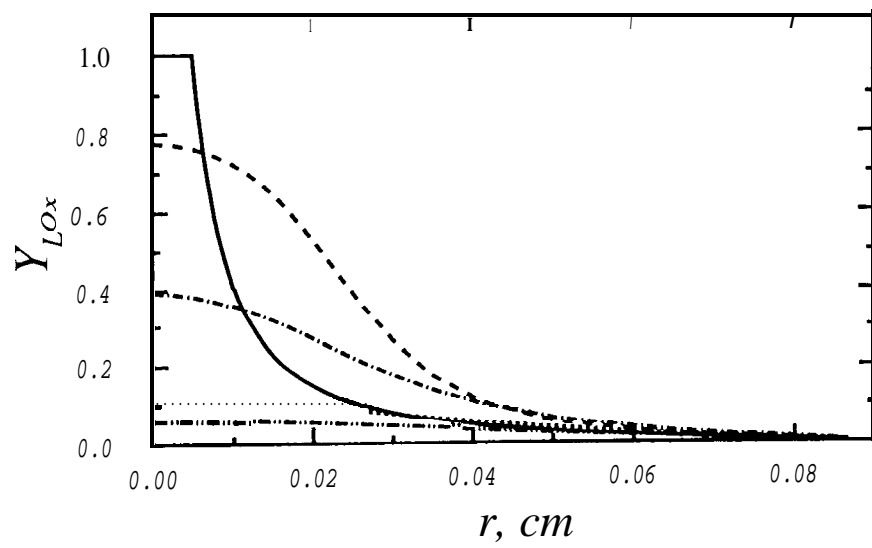


Fig 4

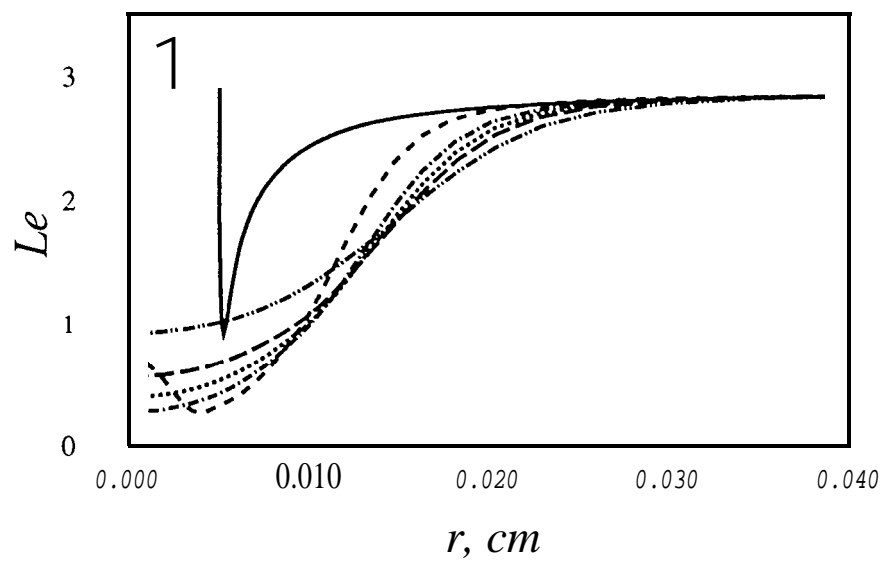


Fig 5a

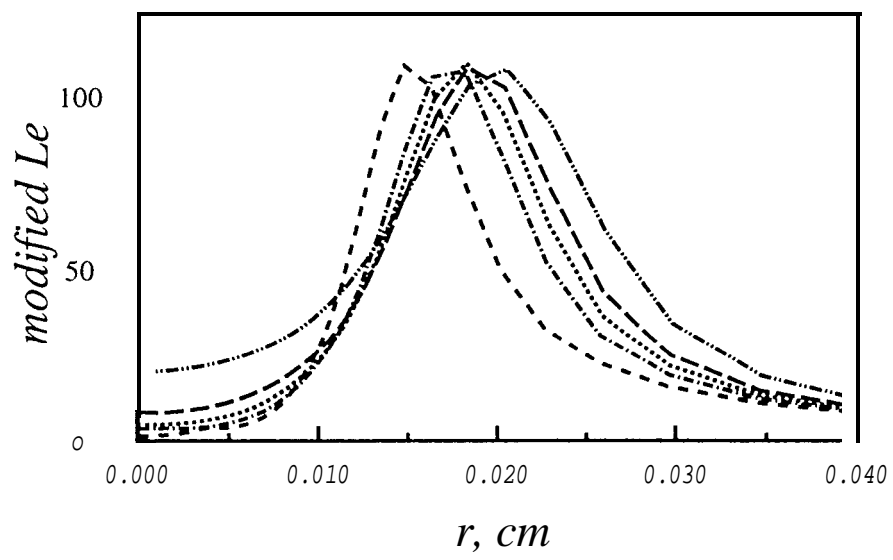


Fig 5b

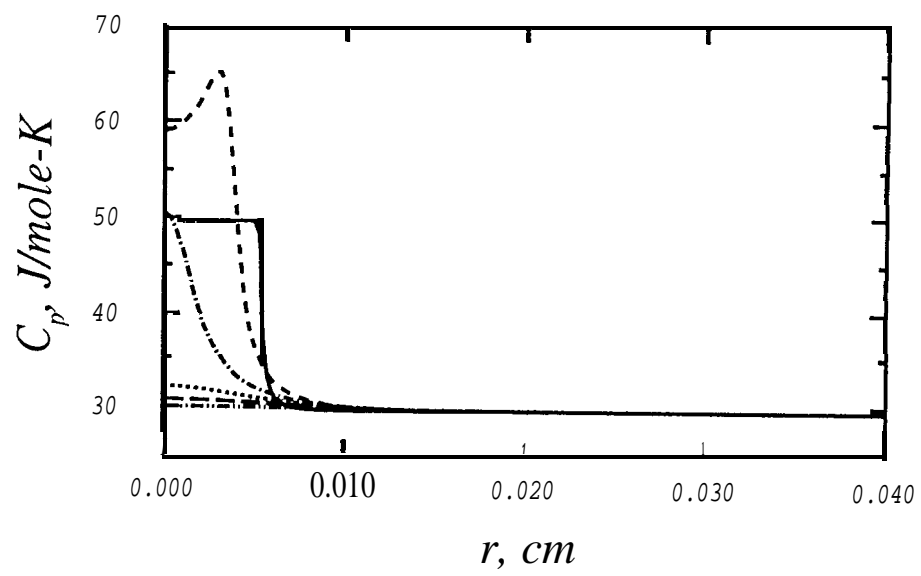


Fig 6a

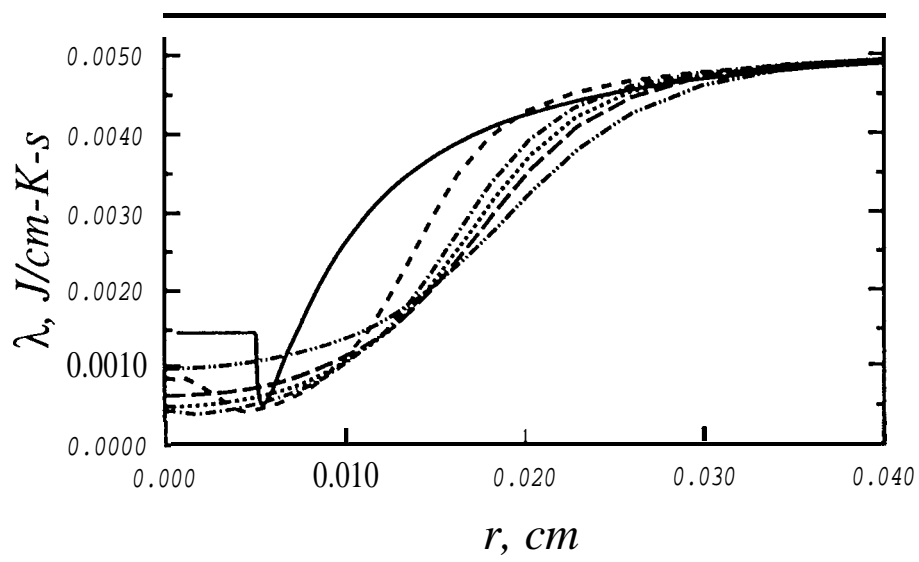
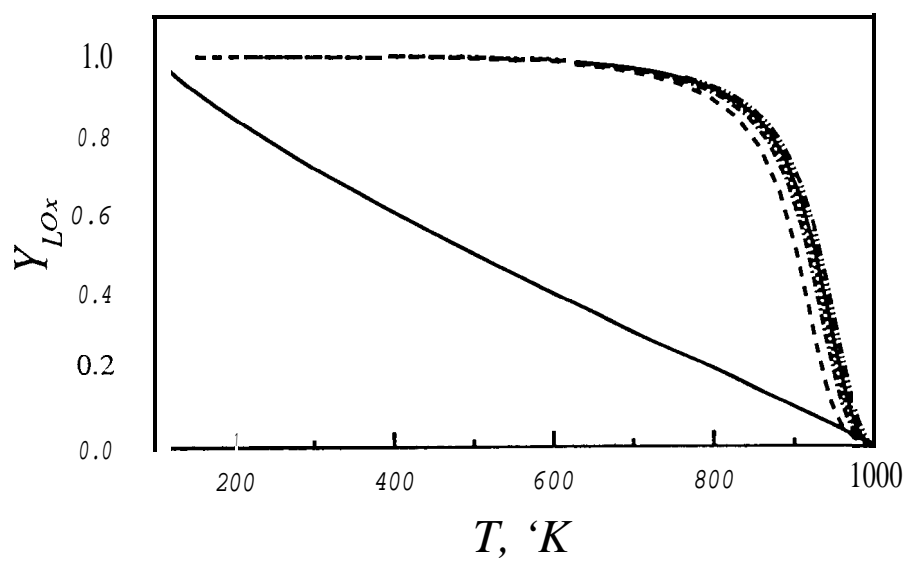
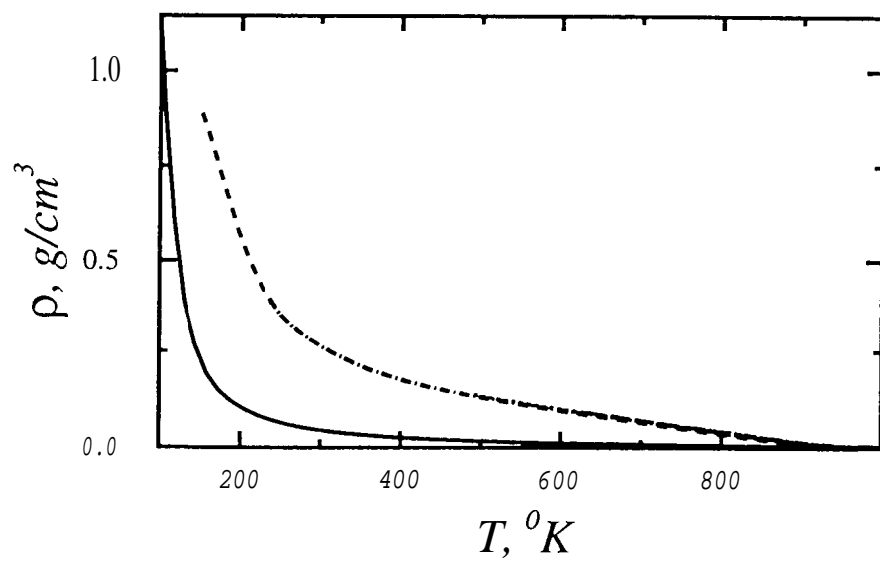


Fig 66







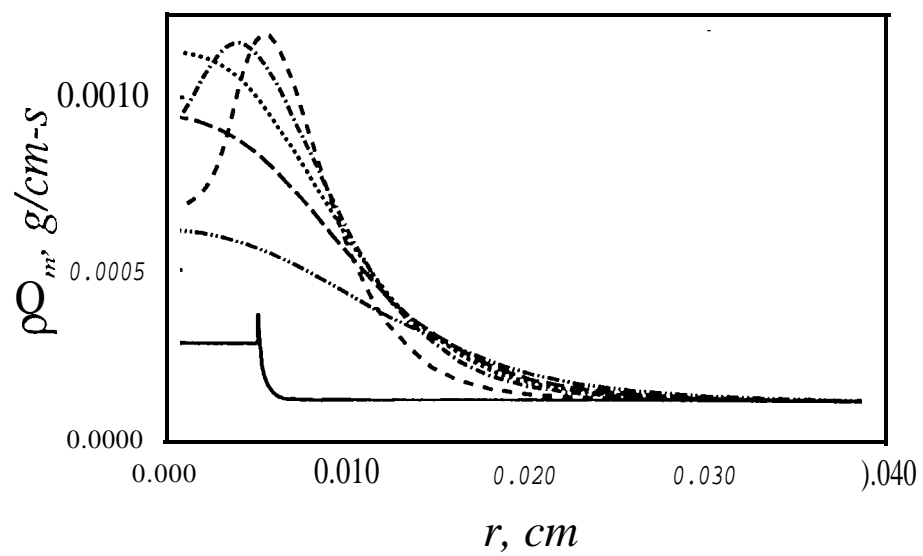


Fig 9

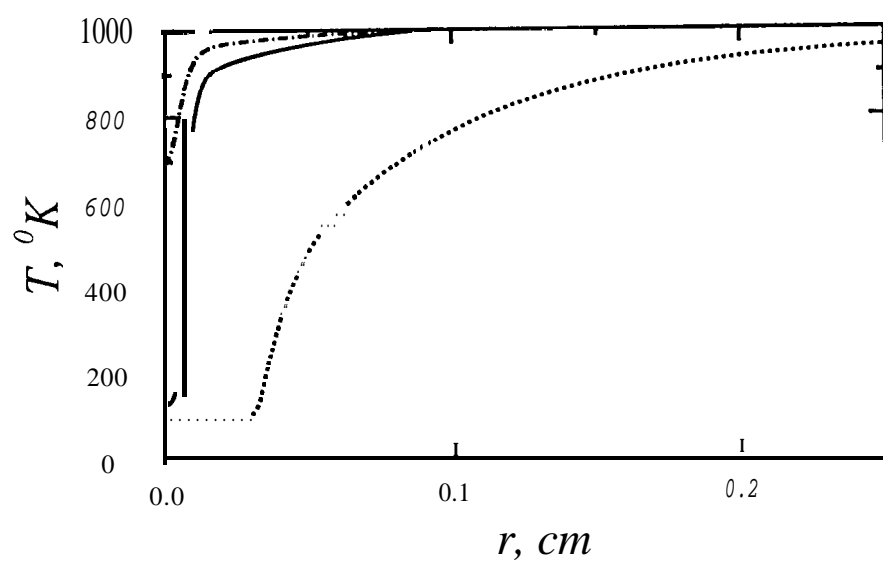
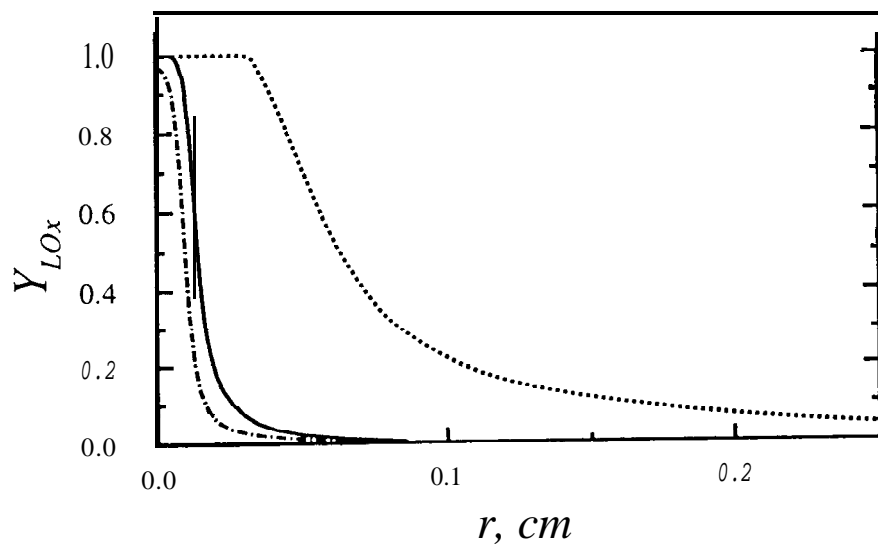
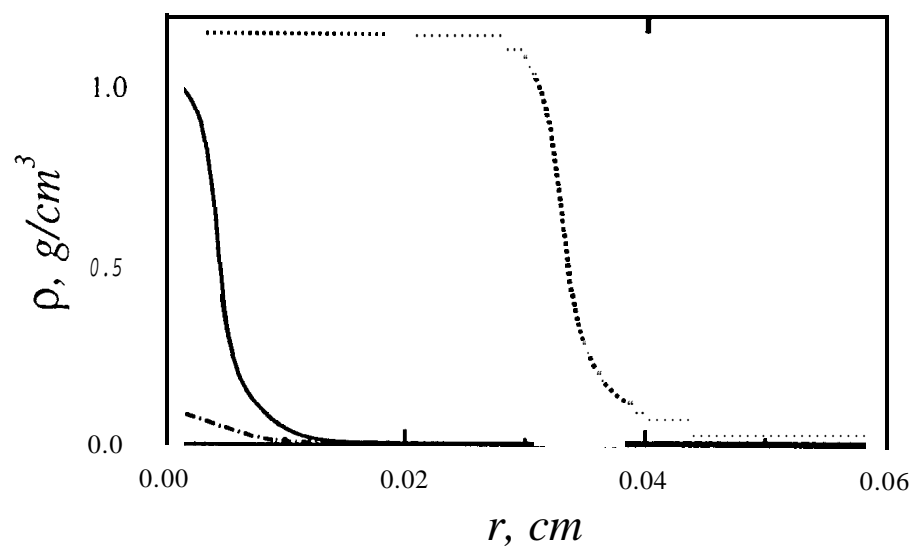


Fig 10a.





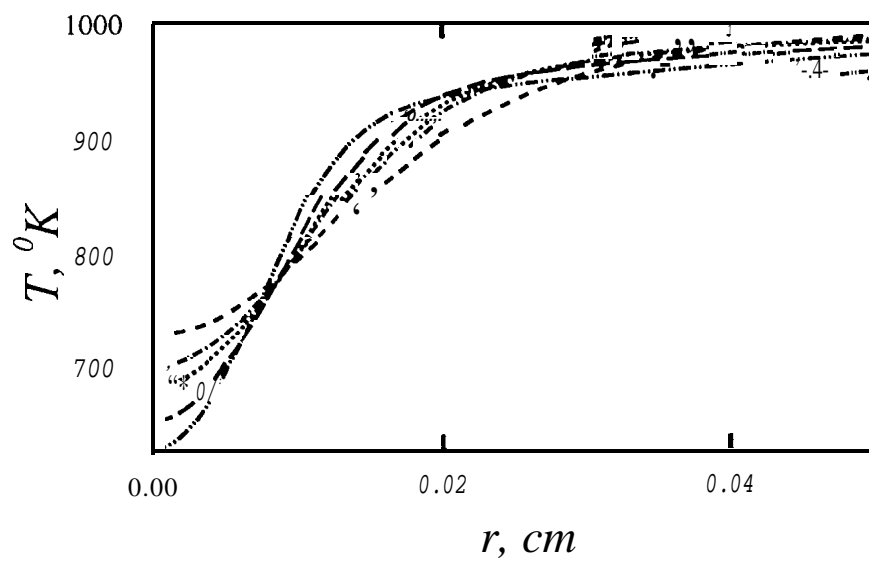
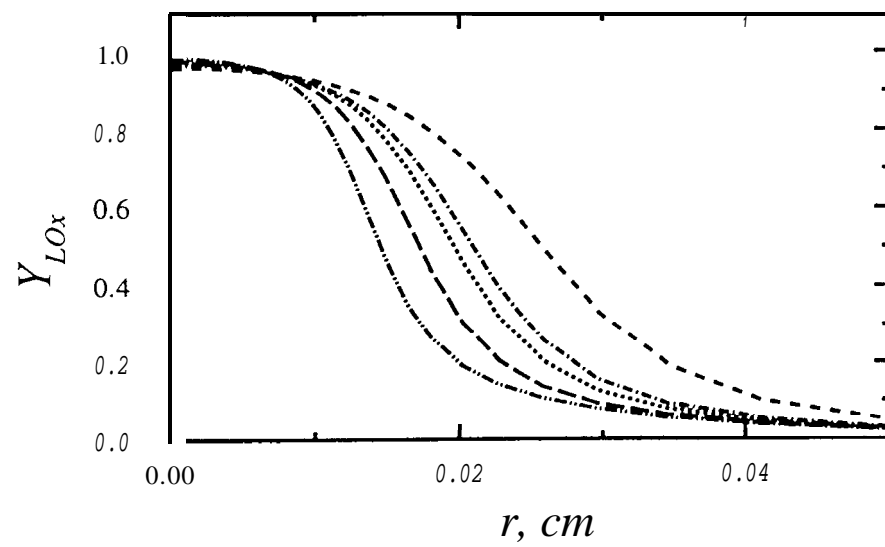


fig 11a



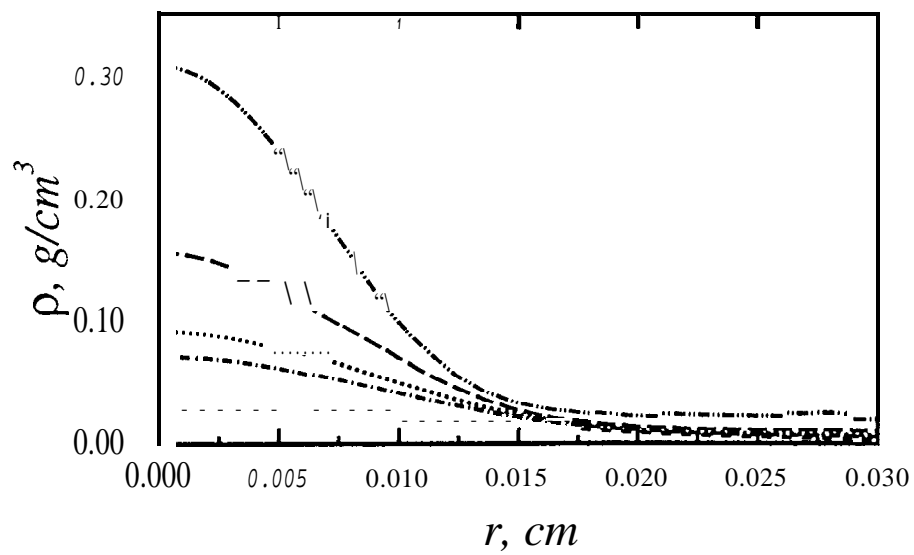
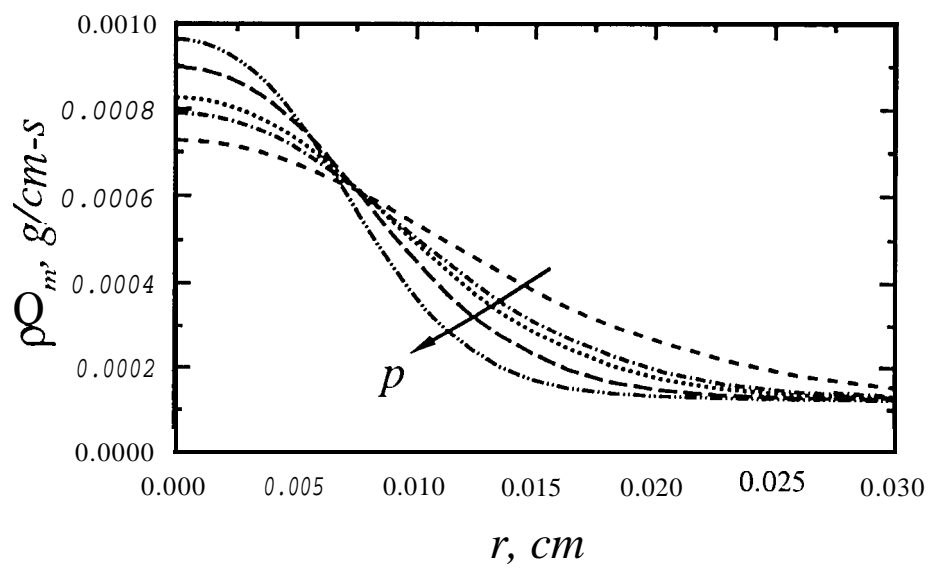


Fig 11c





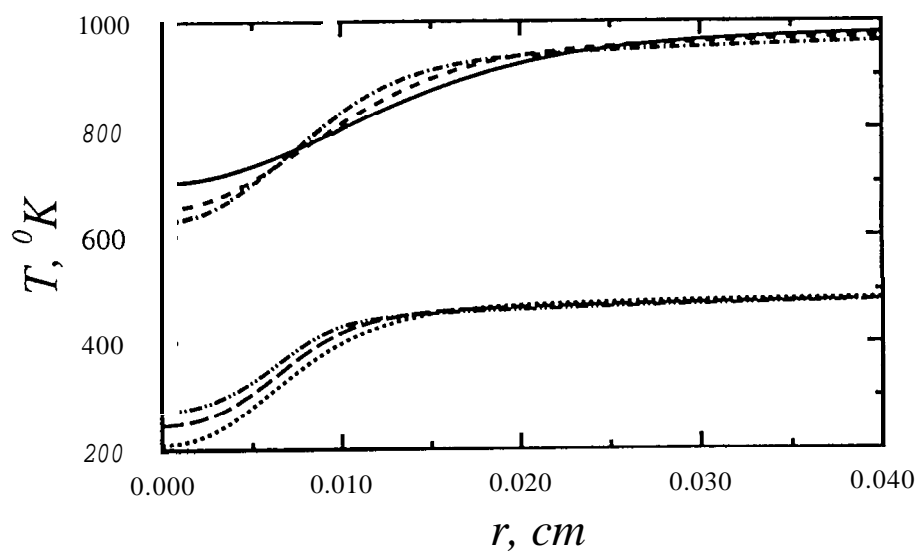


Fig 13a

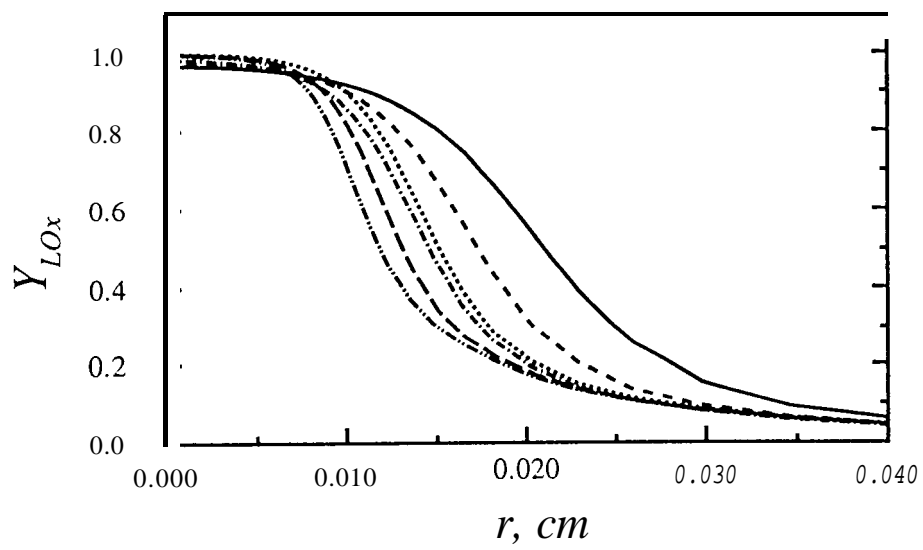


Fig 13b

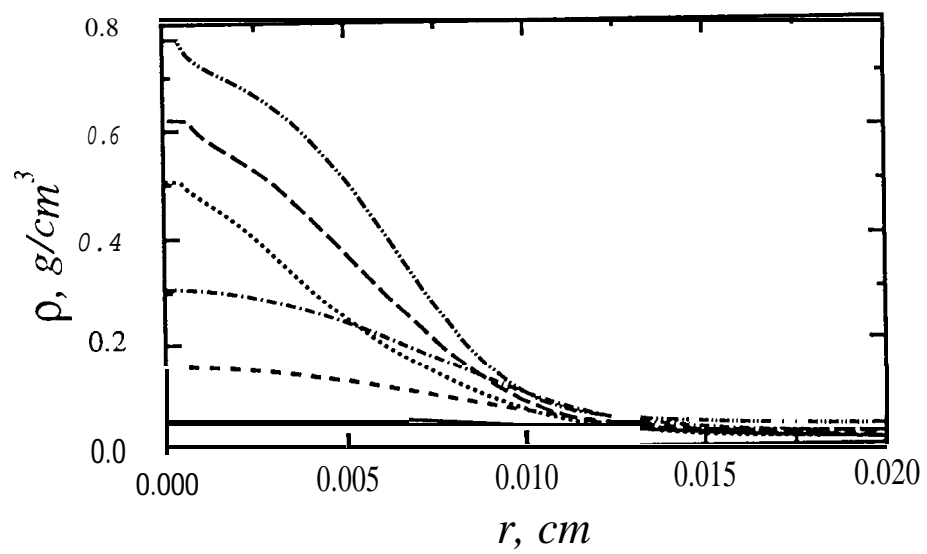


Fig 13c